The in situ formation of ZnS nanodots embedded in honeycomb-like N-S co-doped carbon nanosheets derived from waste biomass for use in lithium-ion batteries

YU Qiu-xiang[1], LI Huan-xin[1,2,*], WEN Yong-liang[1], XU Chen-xi[1], QIN Shi-feng[1], KUANG Ya-fei[1], ZHOU Hai-hui[1,*], HUANG Zhong-yuan[1,*]

（1. *College of Chemistry and Chemical Engineering*, *Hunan University*, *Changsha*, *Hunan* 410082, *China*;
2. *Department of Engineering*, *University of Cambridge*, *9 JJ Thomson Avenue*, *Cambridge*, *CB3 0FA*, *UK*）

Abstract： A nanocomposite of zinc sulfide nanodots imbedded in honeycomb-like N-S co-doped carbon nanosheets (ZnS/NS-CN) was synthesized from waste biomass orange peel using $ZnCl_2$ as the hard template and zinc source, and melamine and thiourea as the respective nitrogen and sulfur sources. When used as the anode material in Li-ion batteries, ZnS/NS-CN has a high reversible capacity (853.5 mAh g^{-1} at 0.1 A g^{-1} after 300 cycles), an excellent long-term cycling stability (70.1% capacity retention after 1 000 cycles at 5 A g^{-1}) and an outstanding rate capability. Besides, a ZnS/NS-CN//$LiNiCoMnO_2$ full cell tested at 0.5-4 V has an excellent battery performance (140.4 mAh g^{-1} at 0.2 C after 150 cycles with an energy density of 132.4 Wh kg^{-1}).

Key words: ZnS nanodots; N-S co-doped carbon nanosheets; Waste biomass; Li-ion batteries

1 Introduction

Enormous efforts have been devoted to the development of new energy storage devices, among which, rechargeable batteries such as LIBs have been extensively investigated as one of the most promising candidates for powering electronics due to their desirable theoretical capacity, high energy density, satisfactory reversibility and reasonable manufacturing cost. Nevertheless, some challenges like the actual capacity being generally far below the theoretical value, the instability under high current conditions, and the pollution caused by raw materials, paint a grim picture for the future of LIBs[1–5]. Therefore, the exploration of suitable electrode materials for realizing the next-generation of LIBs continues to be a hot research topic[6–11].

Carbon materials (such as graphite, porous carbon and graphene) have numerous advantages that include low price, high electrical conductivity, lower working voltage (*vs*. Li/Li^+) and good cycle stability, which have widely contributed to the growth of commercialized LIBs. Nevertheless, the relatively low specific capacity ($\leqslant$372 mAh g^{-1}) and inferior rate capability still hinder their further application in the next-generation high performance energy storage devices[6–7, 9, 12]. Meanwhile, a series of metal oxides, sulfides, selenides and phosphides with high theoretical specific capacity and abundant resources have been researched as electrode materials of LIBs. But their cycling stability and rate performance are less than satisfactory, mainly due to their poor electronic conductivity and the structural collapse of electrodes triggered by huge rate of volume change during electrochemical cycling.

In regard to the above issues, one of the effective strategies is to combine these transition metal compounds with carbon materials, which can not only integrate their advantages, but also make up for their shortcomings. There have been many successful examples of preparing transition metal compounds/carbon materials composites with high capacity, good

Received date: 2022-07-11； **Revised date:** 2022-11-07

Corresponding author: LI Huan-xin. E-mail: hl583@cam.ac.uk;
ZHOU Hai-hui. E-mail: haihuizh@163.com;
HUANG Zhong-yuan. E-mail: zhongyuan.222@163.com

Supplementary data associated with this article can be found in the online version.

rate performance and cycle stability when applied as LIBs electrode materials. For instance, He et al.[13] synthesized carbon-encapsulated Fe_3O_4 nanoparticles uniformly embedded in porous 2D graphitic carbon nanosheets with the help of NaCl particles, the electrode material showed outstanding cycling stability at a high rate (556 mAh g^{-1} at 10 C after 350 cycles). Zhang et al.[14] synthesized Ni_3S_2 inside CMK-3 by using SBA-15 as the template. CMK-3-Ni_3S_2 displays a high capacity of 520 mAh g^{-1} after 100 cycles at 1 A g^{-1}. Ding et al.[15] prepared N-doped multi-shelled hollow Co_3O_4@carbon microspheres electrode which exhibits an ultra-high reversible capacity of 1 701 mAh g^{-1} at 0.1 A g^{-1} after 60 cycles. These examples elucidate the importance of preparation methods and the morphologies of the composites for preparing high-quality carbon/transition metal compound composite electrode materials for LIBs. Only by giving full play to the advantages of the two materials, can the best synergistic effect be achieved.

Recently, biomass-based carbon materials have attracted extensive attention due to their biodegradability, non-toxicity, regeneration and low cost[5, 16]. As carbon precursors, biomass materials usually have naturally porous or hierarchical structures. Through a direct pyrolysis treatment, these structures can be inherited, which can enlarge solid-liquid contact area and speed up ion migration during the electrochemical process[17–19]. At the same time, the defects such as vacancies, edges and heteroatoms can be introduced into the biomass-derived carbon, resulting in more active sites and an improved electric conductivity of the material. Moreover, many biomass materials are recycled from wastes in the traditional industrial and agricultural production processes, so the research and utilization of biomass materials are beneficial to the development of sustainable green and clean energy[20–21].

In this work, waste biomass material was employed as the carbon source precursor. The ZnS/N-S co-doped carbon nanocomposite was successfully synthesized by the calcination of the mixture of orange peels powder, melamine, thiourea and $ZnCl_2$, and then by an etching treatment in hydrochloric acid to remove excess impurities. Through careful design of the preparation process, ZnS with the nano-dot size is embedded in N, S co-doped carbon nanosheets. It not only increases the electrochemical capacity of the anode material, but also avoids the large volume variation of ZnS under the electrochemical process, and enhances the cycle stability and rate performance of the composite material.

2 Experimental

2.1 Sample preparation

For the synthesis of hierarchical honeycomb-like ZnS nanodots/N-S co-doped carbon nanosheets, the orange peels were washed first and dried in a freeze dryer afterwards for 12 h. They were then ground into a fine powder (~ 50 μm) by a mechanical grinder to make orange peel powder.

After that, 1 g of dried orange peel powder was evenly dispersed into 50 mL of deionized water, and then 0.5 g melamine and 0.5 g thiourea dissolved in deionized water of 50 mL were put into the above suspension and agitated at 25 °C for 2 h. Then, the mixture was dried up at 60 °C in a constant temperature oven. The dried mixture was ground together with 3.0 g $ZnCl_2$ and sintered at 900 °C for 2 h in an Ar atmosphere at 5 °C min^{-1}. The final product, ZnS/NS-CN was collected after an etching treatment in 3.0 mol L^{-1} HCl solution for 24 h. For comparison, pure N-S co-doped carbon nanosheets material (NS-CN) was prepared through the above procedure without the presence of $ZnCl_2$. And bare orange peel biomass carbon (OPBC) was also obtained by direct carbonization of the orange peel powder without any chemicals, followed by an acid-washing.

2.2 Characterizations

SEM (Hitachi S-4800, Japan) and TEM (JEM-2100F, Japan) were employed to investigate the morphologies and microstructure. HRTEM and EDS mapping were acquired with an energy dispersive spectrometer on the TEM machine mentioned above. X-ray

powder diffraction (XRD, Bruker D8 Advance, Germany, Cu-*K*α radiation source) was conducted for crystalline structural analysis. The Micromeritics instrument (Tristar ASAP 2020m USA) was employed to evaluate the specific surface area and the pore size distribution of the obtained material. XPS data were processed with an ESCALAB250Xi XPS spectrometer using Al *K*α radiation as the X-ray source. Thermogravimetric analysis (TGA) was used to determine the N-S co-doped C and ZnS contents of the final composite in an air atmosphere.

2.3 Electrochemical measurements

Electrochemical tests were conducted in 2032 type coin cells which were composed of the obtained electrode, a polypropylene membrane (Celgard) as a separator, and a Li foil as the counter electrode, 1 mol L^{-1} $LiPF_6$ dissolved in EC/DEC (1∶1 vol ratio) as electrolyte. The cell assemblies were conducted in an Ar-filled glovebox with extremely low water and oxygen content. The anode electrodes were prepared by uniformly coating dense slurry onto a Cu foil. The slurry was made by a mixture of active material, acetylene black, and poly-vinylidene fluoride (PVDF) binder (8∶1∶1 by weight) in N-methyl-2-pyrrolidinone (NMP) solvent. Then the electrode foil was dried in a vacuum oven at 60 °C for 12 h. The mass densities of active materials in the negative and positive electrodes were 1.5 and 9 mg cm^{-2}, respectively.

The galvanostatic discharge-charge measurements were performed by a LAND-CT2001A battery test system (Shanghai, China). CV tests were executed with a CHI660e electrochemical workstation. Electrochemical impedance (EIS) analyses were performed over a frequency range of 100 kHz to 0.01 Hz.

3 Results and discussion

Fig. 1 depicts the schematic diagram of the fabrication of ZnS/NS-NC. First, the fresh orange peels were thoroughly rinsed and subsequently dried in a freeze dryer for 12 h. Through the freeze-drying of biomass, the orange peel maintains the natural porous structure after dehydration, which is conducive to the insertion of thiourea and melamine solution into its crevice. The freeze-dried orange peels were grounded into powders and mixed with melamine and thiourea solution. Second, the orange peel powders were ground with melamine, thiourea and $ZnCl_2$, forming a homogenous precursor. Third, the mixture was heated at 900 °C under an Ar atmosphere. After calcination at 900 °C, a large number of gases produced by the above mixture are beneficial to the formation of porous honeycomb-like carbon materials and are also favorable to the doping process of N and S into carbon. In the pyrolysis process, the main carbon precursor orange peels powder underwent a carbonization process, along with high-temperature chemical reactions of thiourea, melamine and $ZnCl_2$ templates. The thiourea was first decomposed at ~ 150 °C, which not only introduced the S element in the carbon matrix but also worked as the raw material to react with Zn^{2+} for the formation of ZnS. At about 300 °C, the $ZnCl_2$ started melting and a small content of ZnS was trapped inside the carbon nanosheets during the decomposition of thiourea. Then the melamine also began to decompose with a large production of ammonia, resulting in favorable pores and N-doping in carbon. Meanwhile, $ZnCl_2$ was incrementally transformed to ZnO. As the temperature rises to 600 °C, carbon begins to form *in-situ*, which could further reduce ZnO to Zn metal.

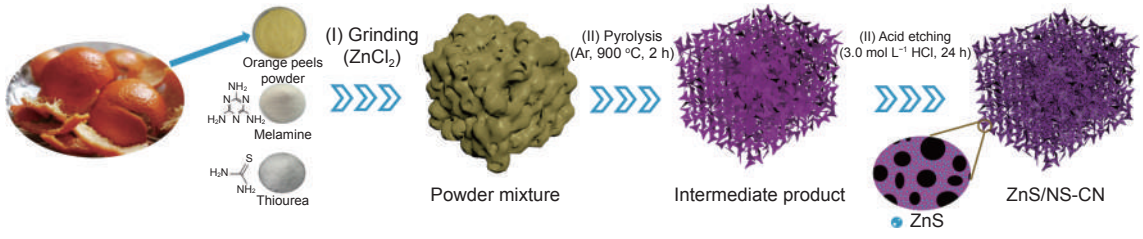

Fig. 1　Schematic illustration for in situ formation of ZnS nanodots embedded in honeycomb-like N-S co-doped carbon nanosheets (denoted as ZnS/NS-CN)

Sublimable Zn metal was released in the form of vapor, forming a hierarchical porous structure containing many micro-, meso- and macro-pores. By adding HCl to the obtained calcined product, the redundant metal oxides and sulfides loaded on the surface of the porous honeycomb-like carbon matrix were removed. At the same time, ZnS dots embedded into the carbon nanosheets were hardly etched by HCl due to the protection of the carbon nanosheets. Finally, the ZnS/NS-CN was obtained by washing and drying in a vacuum oven.

The detailed morphologies of OPBC, NS-CN and ZnS/NS-CN are shown in Fig. 2. Fig. 2a-c reveals that OPBC is a stacked block material with a smooth surface. Without the addition of $ZnCl_2$, NS-CN was obtained (Fig. 2d-f), which breaks into nanosheets due to the decomposition of melamine and thiourea. As shown in Fig. S1, the ZnS/NS-CN before acid etching maintains a porous structure and a rough surface loaded with many nanoparticles. After the acid etching treatment, the images of as-obtained ZnS/NS-CN in Fig. 2g-i show that the sample has a hierarchical porous honeycomb-like structure consisting of 3D interconnected carbon nanosheets.

TEM image of the ZnS/NS-CN in Fig. 3a further confirm the porous honeycomb-like structure. The HRTEM images in Fig. 3b and 3c demonstrate the amorphous state of carbon and low crystalline state of ZnS. The lattice spacing is determined to be ~0.271 nm, which corresponds to the (105) plane of the ZnS phase. Unexpectedly, the carbon lattice stripes can be seen to be more disordered and the spacings between layers (0.421, 0.421, 0.454 and 0.487 nm) of ZnS/NS-CN are far wider than that of graphite (0.336 nm), suggesting the incorporation of N, S and ZnS nanodots increase the carbon layer spacing. Meanwhile, HADDF-STEM was also carried out to study the elemental distribution. The TEM image (Fig. 3d) and the corresponding EDX mapping of C, N, S and Zn clearly show that ZnS nanodots are uniformly distributed in the porous honeycomb-like nanostructure C backbones. The constructed nanoarchitecture is cru-

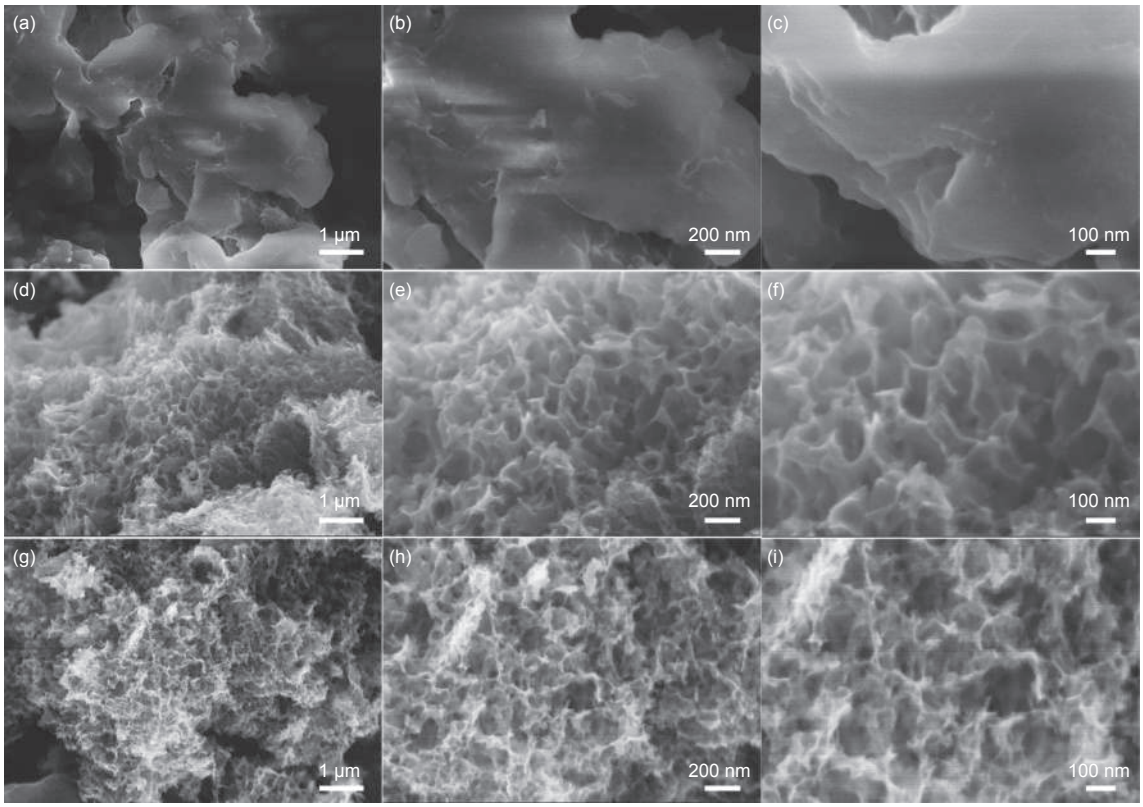

Fig. 2 SEM images of (a-c) OPBC, (d-f) NS-CN and (g-i) ZnS/NS-CN

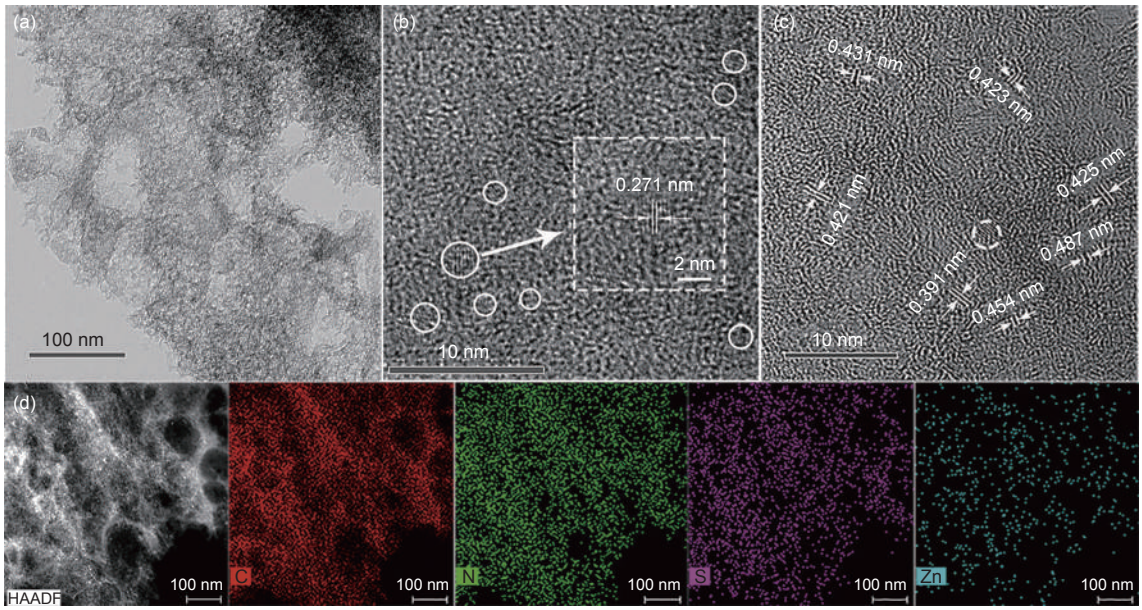

Fig. 3　(a) TEM image, (b,c) HR-TEM images, (d) HADDF-STEM image of ZnS/NS-CN and corresponding elemental mapping of C (red), N (green), S (purple) and Zn (blue)

cial. The carbon matrix is beneficial to improving overall electrode conductivity and keeping the integrity of the electrode. The ultrasmall ZnS nanodots surrounded by high-conductive C tend to show high lithium storage activity and reduce the volume expansion during lithiation/delithiation processes. More than that, the porous honeycomb-like structure and the incorporation of N/S components are anticipated to provide much more defects and active sites, resulting in fast electron transport and Li-ion diffusion, thus the electronic conductivities and total Li^+ storage capacities of the sample are effectively improved[22].

Fig. 4a presents the XRD patterns of the OPBC, NS-CN and ZnS/NS-CN. The XRD patterns of both OPBC and NS-CN have two wide peaks located at 22.0° and 44.0°, ascribed to (002) and (101) planes of graphitic carbon, respectively. As for ZnS/NS-CN, the peaks at 26.9°, 28.5°, 30.4°, 33.0°, 47.7°, 52.0°, 56.5°, 58.6°, 69.5°, 76.8° and 79.3° were identified to (100), (008), (104), (105), (110), (1012), (118), (205), (1017), (213) and (1116) of wurtzite ZnS (JCPDS No. 39-1363)[23–24]. Additionally, a broad peak of ZnS/NS-CN is displayed at about 21°, corresponding to amorphous carbon[25]. To explore the composition of the calcined product and the role of pickling, the XRD pattern of ZnS/NS-CN before acid etching is also obtained in Fig. S2. By comparison, the peak intensity after pickling becomes lower, and the peaks of ZnO and part of the peaks of ZnS disappear. The chemical composition and element valence states of ZnS/NS-CN are verified by XPS analysis. In accordance with the EDX mapping analysis, pronounced C 1s, N 1s, S 2p and Zn 2p peaks are noticed in Fig. 4b. The spectrum (Fig. 4c) of C 1s could be resolved into 3 separate peaks which are aligned with C—C (284.8 eV), C—N/S (285.7 eV) and C—O (289.3 eV), revealing the chemical bonding between heteroatoms and carbon nanosheets[26]. The spectrum of N 1s can be fitted into 4 peaks, namely, the graphitic N (401.1 eV), pyridinic N (398.4 eV), pyrrolic N (399.4 eV) and oxidized N (404.5 eV), as shown in Fig. 4d[27]. The existence of S is also depicted by the S 2p spectrum in Fig. 4e. The peaks positioned at 161.8 eV and 162.5 eV are characteristic of S $2p_{3/2}$ and S $2p_{1/2}$ of S^{2-} in ZnS, while the other two fitting peaks at 163.9 and 164.8 eV are assigned to C—S bonds of thiophenic S, suggesting the successful incorporation of S-heteroatoms[28]. Furthermore, the apparent peak at 168.5 eV is ascribed to the S—O and S=O bonds generated from sulfur oxidation in air[27]. In Fig. 4f,

Zn 2p spectrum shows 2 main peaks at 1 022.4 and 1 045.5 eV which can be belonging to Zn $2p_{3/2}$ and Zn $2p_{1/2}$[28].

In addition, N_2 adsorption-desorption isothermal methods were conducted to further examine the specific surface areas and pore size distribution of ZnS/NS-CN (Fig. 5a). The corresponding isotherm in Fig. 5a can be categorized as a typical type IV isotherm model with an H4 hysteresis loop, indicating the existence of porous structures. Concurrently, the specific surface area is calculated to be 291.9 $m^2\ g^{-1}$ based on the N_2 adsorption-desorption curve. The BJH plot in the inset displays that the diameter of the pores mainly concentrates on ~1.33 and ~45.2 nm, which indicates that the ZnS/NS-CN composite possesses large number of mesoporous channels. Moreover, the amount of NSC in ZnS/NS-CN composite was evaluated by the thermogravimetric analysis (TGA) performed from 24 to 900 °C at 10 °C min^{-1} in air. As displayed in Fig. 5b, the weight loss in area I from 24 to 270 °C mainly results from the evaporation of adsorbed water. The slope line from 270 to 435 °C suggests that the oxygen-containing functional groups are dislodged from the carbon nanosheets. The evident weight loss (area III) between 435 and 900 °C is assigned to the conversion of ZnS into ZnO and the

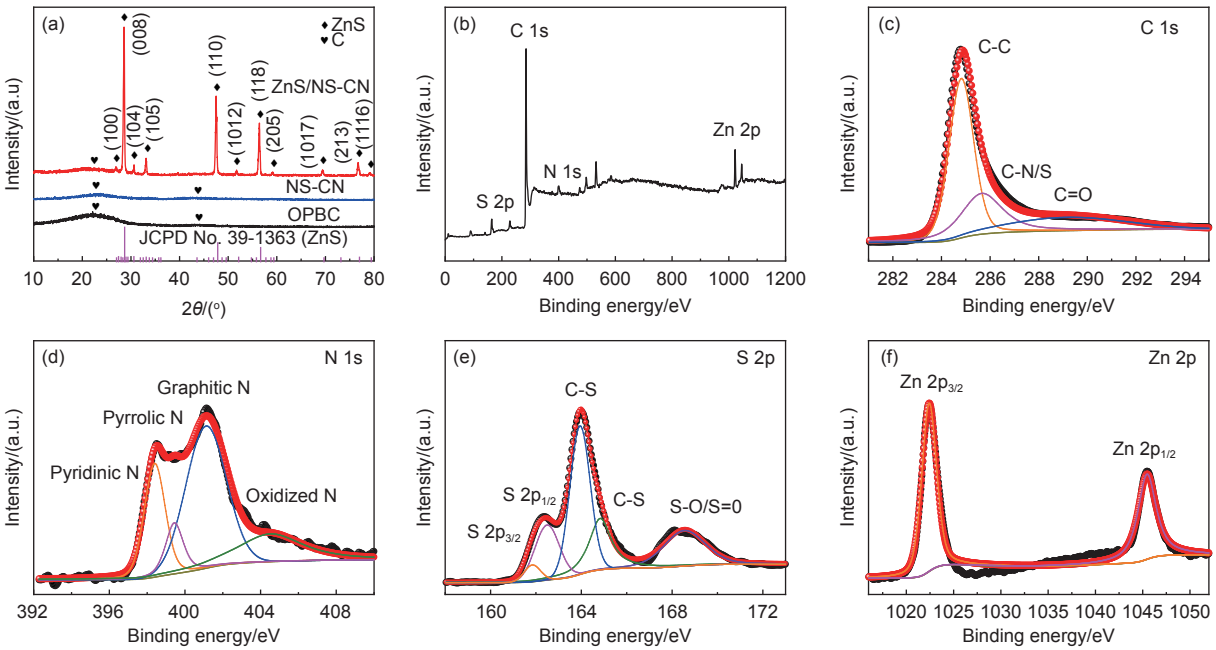

Fig. 4 (a) XRD patterns of OPBC, NS-CN, ZnS/NS-CN. (b) XPS survey spectrum of ZnS/NS-CN. High resolution XPS spectra of (c) C 1s, (d) N 1s, (e) S 2p, (f) Zn 2p of ZnS/NS-CN

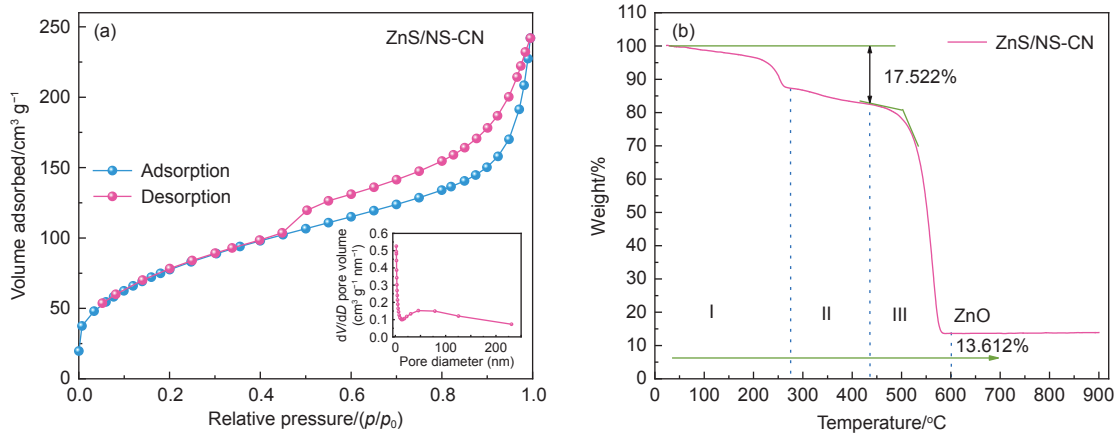

Fig. 5 (a) N_2 adsorption−desorption isotherm curve and pore size distribution (inset) of ZnS/NS-CN. (b) TGA curve of the ZnS/NS-CN composite

combustion of N-S co-doped carbon nanosheets. Therefore, the content of ZnS is roughly calculated to be 19.8% in the composite based on the amount of ZnO in the final material composition[28–29].

The electrochemical properties of ZnS/NS-CN were evaluated as electrodes for LIBs. Fig. 6a displays the CV curves of ZnS/NS-CN electrodes for the first 4 cycles, which are acquired in a potential range of 0.01-3.0 V at 0.1 mV s^{-1}. In the initial scan, the reduction peaks at ~1.68 and 0.66 V correspond to the voltage platforms during the first discharge process in Fig. 6b, which is ascribed to the conversion reaction of ZnS to metal Zn/Li_2S and Zn-Li alloying reaction[29]. The small reduction peak at 1.20 V could be related to the transformation reaction and the growth of solid electrolyte interface (SEI) film[30]. In the following anodic process, the oxidation peaks observed at 0.55, 0.67 and 1.37 V are mainly assigned to the multistep oxidation or de-lithiation process of Li-Zn alloys and the typical reversible production of ZnS originating from Zn and Li_2S, respectively[31–32]. In addition, two extra oxidation peaks at 1.89 and 2.38 V in all probability arise from the reaction between Li_2S and S or little impurity (ZnO) mixed in the ZnS/NS-CN composite[33]. It is noteworthy that the subsequent CV profiles are highly overlapped, indicating the good electrochemical reversibility of the ZnS/NS-CN composite.

The galvanostatic charge-discharge plots of the ZnS/NS-CN electrode for the 1st, 2nd, 100th, 200th and 300th at 100 mA g^{-1} are presented in Fig. 6b. During the 1st cycle, the initial discharge and charge capacities are 1 109.3 and 845.5 mAh g^{-1}, with an initial coulombic efficiency of 76.2%. Interestingly, with increasing number of cycles, the discharge capacity decreases to 763.1 mAh g^{-1} after 100 cycles and then gradually increases back to 853.5 mAh g^{-1} after 300 cycles, which can be attributed to the activation process of ZnS dots. Moreover, the cycling behaviors of the OPBC, NS-CN and ZnS/NS-CN electrodes at 0.1 A g^{-1} over 300 cycles are investigated in Fig. 6c. Not surprisingly, the OPBC shows the lowest capacity of 306.0 mAh g^{-1} after 300 cycles with about 64% capacity retention. In contrast, the discharge capacity of NS-CN is 680.0 mAh g^{-1} after 300 cycles on account of the porous honeycomb-like structure and the co-doping of hybridizing heteroatoms (N, S). As for the ZnS/NS-CN electrode, it delivers a larger discharge capacity and superior cycle stability, which could be assigned to a larger specific surface area and

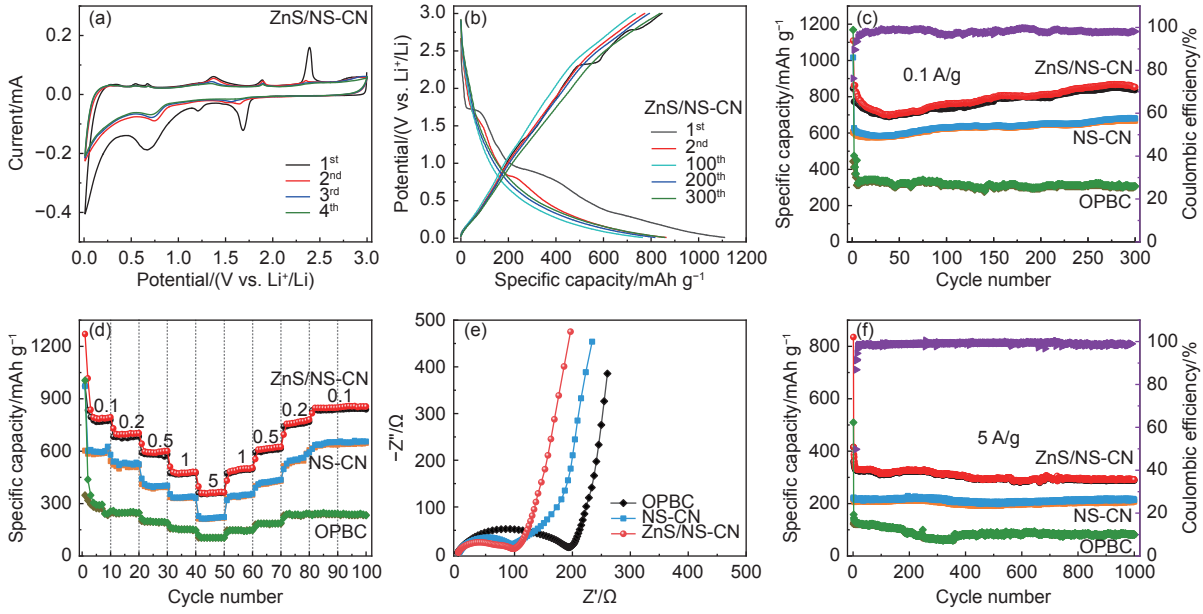

Fig. 6　(a) CV curves of the ZnS/NS-CN anode for the initial four cycles at a scan rate of 0.1 mV s^{-1}. (b) Charge/discharge curves of the ZnS/NS-CN anode for 1st, 2nd, 100th, 200th, 300th cycles. Cycling performance of the ZnS/NS-CN, NS-CN and OPBC electrodes at (c) 0.1 A g^{-1} and (f) 5 A g^{-1}. (d) Rate capabilities at various current densities and (e) EIS plots of the ZnS/NS-CN, NS-CN and OPBC electrodes

abundant bridges. The increase in capacity during cycling can be attributed to the following reasons: (i) Limited by the rate of electrolyte infiltration and diffusion, part of the active material failed to participate in the reaction in the preliminary test, and as the reaction continued, the electrolyte gradually infiltrated the inner part of the active material, making the capacity of the material increase in the later cycle process[34]. (ii) The formation of SEI film in the first cycle leads to a decrease in capacity, but as the number of cycles increases, the pulverization of the active material in the microstructure can also lead to the exposure of some of the active sites that were not involved in the reaction earlier, again manifesting as an increase in capacity during the later cycles[35]. (iii) Since the active material is a composite of doped carbon and transition metal sulfide nanoparticles, the additional lithium-ion storage induced by defects on the doped carbon matrix[36] and the interfacial capacitance between the metal nanoparticles and Li_2O[37] can also lead to an increase in capacity.

The rate capabilities of these 3 samples were studied at various current densities from 0.1 to 5 A g^{-1} (Fig. 6d). Specifically, the ZnS/NS-CN electrode delivers remarkable average discharge capacities of 801, 681, 581, 472 and 359 mAh g^{-1} at 0.1, 0.2, 0.5, 1 and 5 A g^{-1}, respectively, the NS-CN electrode displays slightly lower specific capacities and the OPBC electrode shows the lowest capacities at each current density. When the current density returned to 0.1 A g^{-1}, the capacity of the ZnS/NS-CN and NS-CN electrodes can be recovered to the initial value while a large decay can be found in OPBC, indicating good structural stability of ZnS/NS-CN even at high current density. Additionally, the Nyquist plots of the electrodes before cycling are illustrated in Fig. 6e. Compared with OPBC, due to the existence of an S-N co-doping conductive carbon network, the ZnS/NS-CN and NS-CN electrodes manifest a smaller diameter of the semicircle, suggesting a lower Li-ion diffusion impedance. Furthermore, long-term cycling under a high rate applied on the electrodes was evaluated at 5 000 mA g^{-1}(Fig. 6f). The ZnS/NS-CN electrode delivers the highest capacity of ~291.6 mAh g^{-1} and 70.1% capacity retention after 1 000 cycles. In addition, the morphological and structural changes of the ZnS/NS-CN electrode after 1 000 cycles were depicted by SEM and TEM. As displayed in Fig. S3, the honeycomb porous ZnS/NS-CN material agglomerates seriously after long-term cycling, but the nanosheet structure remains identifiable. The TEM images also show that the honeycomb-like porous structure of the composite is well maintained, indicating that it has good structural stability and capacity retention. These results further demonstrate that incorporating honeycomb-like N, S co-doped carbon nanostructure is vital to the improvement of electrochemical capacity and stability, and the addition of ZnS nanodots could offer more capacity for the whole electrode. More than that, our work is one of the best results among those previously reported ZnS-C based anode materials on the lithium storage (Table S1).

To further characterize the superior electrochemical properties of the ZnS/NS-CN for LIBs, the CV curves at various scan rates from 0.3 to 1.5 mV s^{-1} between 0.01 and 3.0 V were obtained as depicted in Fig. 7a. Generally, the relationship between current response and sweep rate follows the formula.

$$i = av^b \quad (1)$$

where a and b are both variable constants[38]. The b = 0.5 represents to a typical diffusion-controlled process, whereas b = 1.0 stands for a capacitive-controlled process. As displayed in Fig. 7b, the b values for the redox peaks are calculated to be 0.78, 0.69, 0.81 and 0.75, demonstrating that electrochemical reactions of ZnS/NS-CN contain both the diffusion-controlled and pseudocapacitive-controlled processes. The specific capacitive contribution ratio is further estimated quantitatively based on below equation:

$$i = k_1 v + k_2 v^{1/2} \quad (2)$$

in which $k_1 v$ represents the capacitive behavior and $k_2 v^{1/2}$ the diffusion behavior, respectively[39–40]. By calculating the k_1 and k_2 values, the capacitive charge contribution is 47.9% of the total capacity at 0.3 mV s^{-1} in Fig. 7c. With the scan rate increases, the capacitive contribution gradually increases from

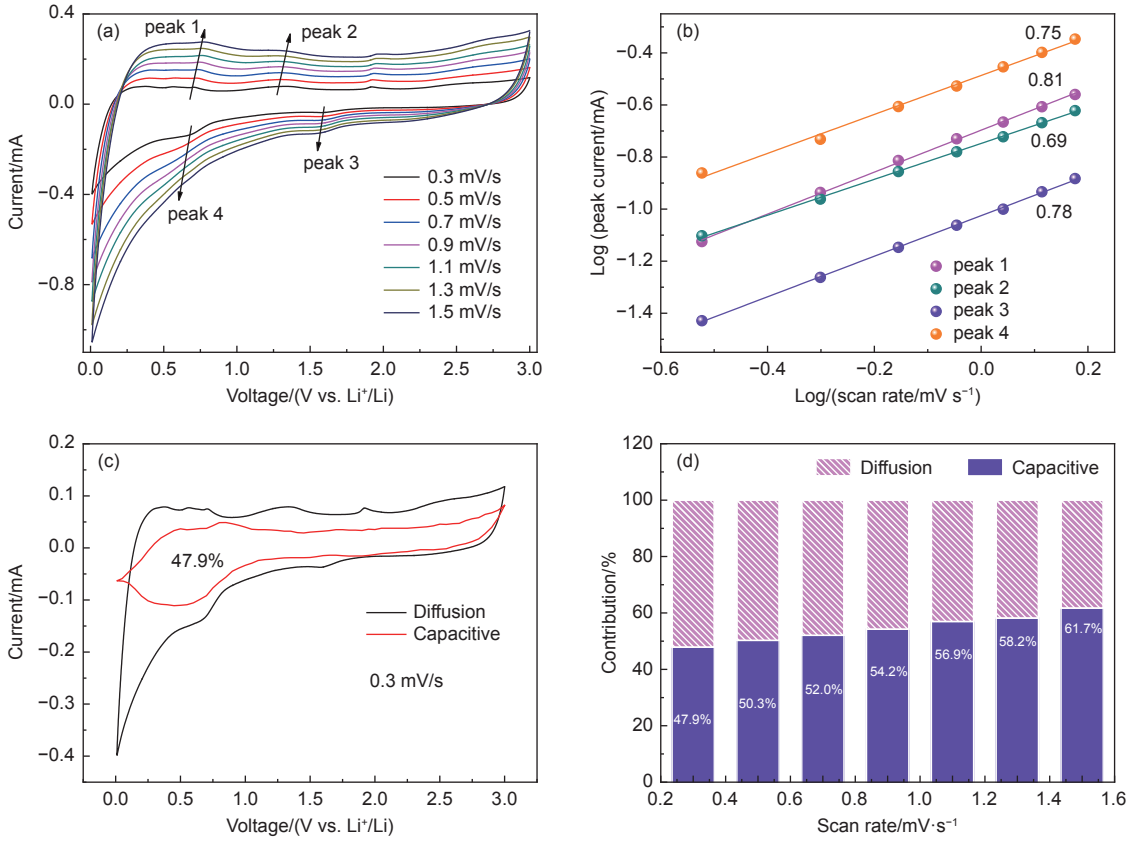

Fig. 7　(a) CV curves of ZnS/NS-CN at scan rates from 0.3 to 1.5 mV s^{-1}. (b) *b* value determination for anodic process. (c) Capacitance contribution (pink) and diffusion contribution (violet) at 0.3 mV s^{-1}. (d) The capacitance contribution ratio at increasing scan rate from 0.3 to 1.5 mV s^{-1}

47.9% to 61.7% at 1.5 mV s^{-1} (Fig. 7d). The increasing capacitive-controlled contribution is induced by abundant defects and active sites originating from the amorphous carbon nanosheets with abundant voids, N/S co-doped heteroatoms, and ultrasmall ZnS nanodots, which could facilitate the adsorption of Li^+ and hence result in good rate performance[41]. It should be noted that at a low scanning rate, the large pseudo-capacitance is mainly attributed to the porous honeycomb-like structure, which is conducive to electrolyte wetting and facilitates the transfer of electrons/ions[42].

Moreover, to explore its performance for practical applications, the Li-ion full cells were fabricated by assembling the ZnS/NS-CN anode with $LiNiCoMnO_2$ cathode. The electrochemical performance of $LiNiCoMnO_2$ is showed in Fig. S5. To make the cell capacity balance close to the ratio of 1∶1 ratio, the mass ratio of $LiNiCoMnO_2$ to ZnS/NS-CN is determined to be ~3.8∶1 based on their specific capacities (476.2 mAh g^{-1} for ZnS/NS-CN at 1 C, 1 C = 963–1 000 mA g^{-1}; 127.1 mAh g^{-1} for $LiNiCoMnO_2$ at 1 C, 1 C = 280 mA g^{-1}). Fig. 8a exhibits the charge/discharge curves of ZnS/NS-CN//$LiNiCoMnO_2$ full cell after 1, 2, 50, 100 and 150 cycles at 0.2 C in the voltage window of 0.5–4 V in respect of the cathode. The first discharge capacity of 189.1 mAh g^{-1} is obtained and 74.3% of the capacity is retained after 150 cycles in Fig. 8b, suggesting its good cycle stability. Calculated from the 150th discharge curve, the energy density is as high as 132.4 Wh kg^{-1}. In addition, ZnS/NS-CN//$LiNiCoMnO_2$ full cell also shows an excellent rate capability (Fig. 8c). As shown in Fig. 8d, the full cell possesses a low electronic resistance. The cyclic voltammetry curves (Fig. S4) of the full battery shows 2 paired redox peaks (2.05/1.33 V and 2.38/1.98 V), which can be assigned to the following reaction equations:

$$LiNiCoMnO_2 + x/2\ ZnS \leftrightarrow Li_{(1-x)}NiCoMnO_2 + x/2\ Zn + x/2\ Li_2S \quad (3)$$

$$Li_{(1-x)}NiCoMnO_2 + Zn \leftrightarrow Li_{(1-x-y)}NiCoMnO_2 + Li_yZn \quad (4)$$

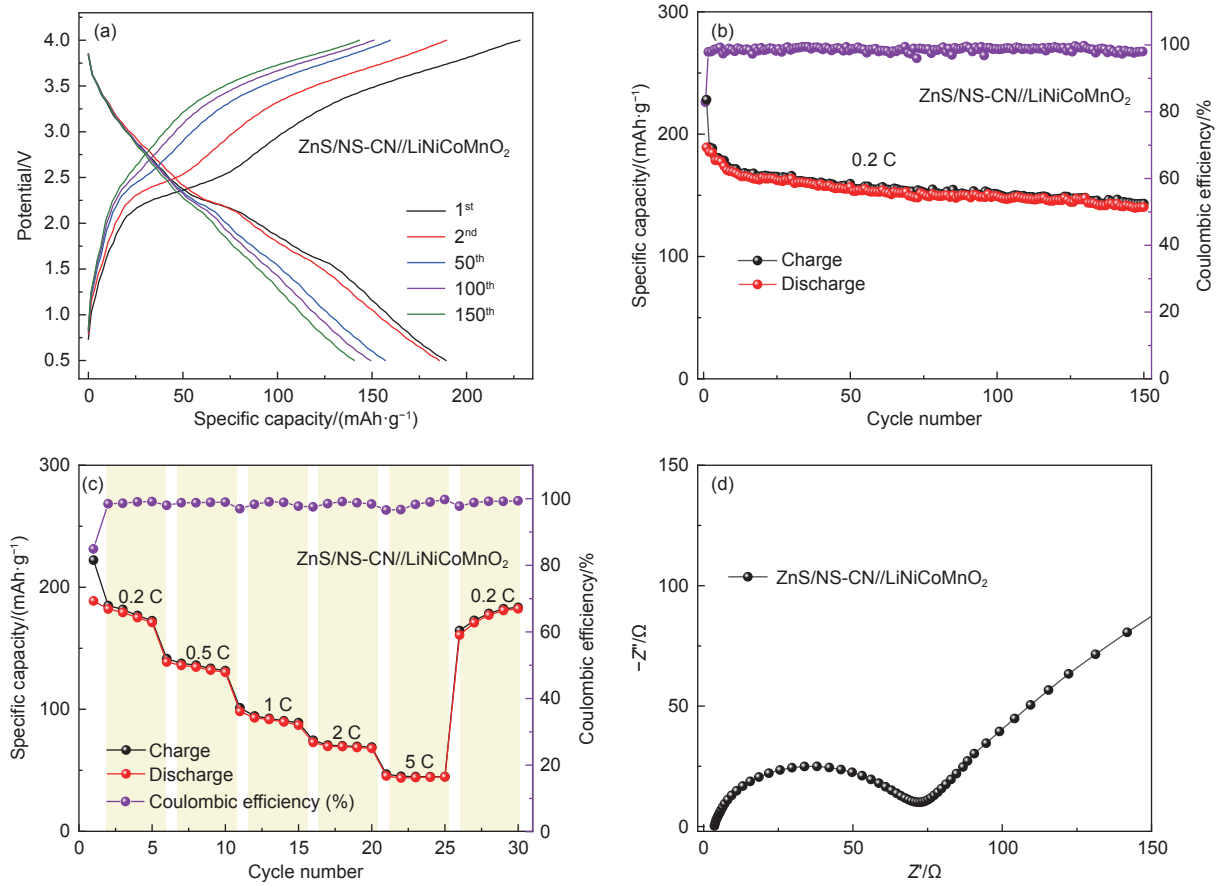

Fig. 8 (a) Charge/discharge curves, (b) cycling performance, (c) rate capability, and (d) EIS plot before testing of the ZnS/NS-CN//$LiNiCoMnO_2$ full cells

4 Conclusion

In summary, the unique ZnS/NS-CN composite was synthesized successfully by facile templating calcination of waste biomass. The composite manifests an excellent reversible capacity of 853.5 mAh g^{-1} over 300 cycles at 0.1 A g^{-1} and an ultrahigh rate capability. In terms of practicality, the full cell test results demonstrated that the designed ZnS/NS-CN composite show great potential as competent electrodes. This work may provide a new route for fabricating ZnS nanodots embedded in honeycomb-like N-S co-doped carbon nanosheets by using low-cost and renewable waste biomass carbon and offer a new simple strategy for the preparation of hierarchical porous structure materials for energy storage.

Acknowledgements

This work was supported by National Natural Science Foundation of China (52274298, 51974114, 51672075, 21908049), China Postdoctoral Science Foundation (2020M682560), Hunan Provincial Natural Science Foundation of China (Grant No. 2020JJ4175), Science & technology innovation program of Hunan Province (2020RC2024) and the Fundamental Research Funds for the Central Universities.

Conflicts of interest

There are no conflicts to declare.

References

[1] Scrosati B, Garche J. Lithium batteries: Status, prospects and future[J]. Journal of power sources, 2010, 195(9): 2419-2430.

[2] Wu F, Maier J, Yu Y. Guidelines and trends for next-generation rechargeable lithium and lithium-ion batteries[J]. Chemical Society Reviews, 2020, 49(5): 1569-1614.

[3] Goodenough J B, Kim Y. Challenges for rechargeable Li batteries[J]. Chemistry of materials, 2010, 22(3): 587-603.

[4] Liu K, Liu Y, Lin D, et al. Materials for lithium-ion battery safety[J]. Science advances, 2018, 4(6): eaas9820.

[5] Chen Q, Tan X, Liu Y, et al. Biomass-derived porous graphitic carbon materials for energy and environmental applications[J]. Journal of Materials Chemistry A, 2020, 8(12): 5773-5811.

[6] Bruce P G, Scrosati B, Tarascon J M. Nanomaterials for rechargeable lithium batteries[J]. Angewandte Chemie International Edition, 2008, 47(16): 2930-2946.

[7] Liu H, Liu X, Li W, et al. Porous carbon composites for next generation rechargeable lithium batteries[J]. Advanced Energy Materials, 2017, 7(24): 1700283.

[8] Du X, Zhao H, Lu Y, et al. Synthesis of core-shell-like ZnS/C nanocomposite as improved anode material for lithium ion batteries[J]. Electrochimica Acta, 2017, 228: 100-106.

[9] Zhang H, Zhao H, Khan M A, et al. Recent progress in advanced electrode materials, separators and electrolytes for lithium batteries[J]. Journal of Materials Chemistry A, 2018, 6(42): 20564-20620.

[10] Zhao Y, Li X, Yan B, et al. Recent developments and understanding of novel mixed transition-metal oxides as anodes in lithium ion batteries[J]. Advanced Energy Materials, 2016, 6(8): 1502175.

[11] Zheng Z, Wu H H, Liu H, et al. Achieving fast and durable lithium storage through amorphous FeP nanoparticles encapsulated in ultrathin 3D P-doped porous carbon nanosheets[J]. ACS Nano, 2020, 14(8): 9545-9561.

[12] Zhang Y, Jiao Y, Liao M, et al. Carbon nanomaterials for flexible lithium ion batteries[J]. Carbon, 2017, 124: 79-88.

[13] He C, Wu S, Zhao N, et al. Carbon-encapsulated Fe_3O_4 nanoparticles as a high-rate lithium ion battery anode material[J]. ACS Nano, 2013, 7(5): 4459-4469.

[14] Zhang S, Lin R, Yue W, et al. Novel synthesis of metal sulfides-loaded porous carbon as anode materials for lithium-ion batteries[J]. Chemical Engineering Journal, 2017, 314: 19-26.

[15] Ding Y, Hu L, He D, et al. Design of multishell microsphere of transition metal oxides/carbon composites for lithium ion battery[J]. Chemical Engineering Journal, 2020, 380: 122489.

[16] Jin C, Nai J, Sheng O, et al. Biomass-based materials for green lithium secondary batteries[J]. Energy & Environmental Science, 2021, 14(3): 1326-1379.

[17] Gong H, Du T, Liu L, et al. Self-source silicon embedded in 2D biomass-based carbon sheet as anode material for sodium ion battery[J]. Applied Surface Science, 2022, 586: 152759.

[18] Liang C, Wang P, Li Y, et al. Biomass based composite used as anode materials: Porous ZnO anchored on the rice husk-derived carbon substrate for Li-ion batteries[J]. Materials Science and Engineering:B, 2022, 278: 115656.

[19] Li H, Gong Y, Fu C, et al. A novel method to prepare a nanotubes@ mesoporous carbon composite material based on waste biomass and its electrochemical performance[J]. Journal of Materials Chemistry A, 2017, 5(8): 3875-3887.

[20] Li T, Zhi D D, Guo Z H, et al. 3D porous biomass-derived carbon materials: Biomass sources, controllable transformation and microwave absorption application[J]. Green Chemistry, 2022, 24(2): 647-674.

[21] John K I, Omorogie M O. Biomass-based hydrothermal carbons for catalysis and environmental cleanup: A review[J]. Green Chemistry Letters and Reviews, 2022, 15(1): 162-186.

[22] Huang M, Mi K, Zhang J, et al. MOF-derived Bi-metal embedded N-doped carbon polyhedral nanocages with enhanced lithium storage[J]. Journal of Materials Chemistry A, 2017, 5(1): 266-274.

[23] Teng Y, Liu H, Liu D, et al. Pitaya-like carbon-coated ZnS/carbon nanospheres with inner three-dimensional nanostructure as high-performance anode for lithium-ion battery[J]. Journal of colloid and interface science, 2019, 554: 220-228.

[24] Dong S, Li C, Li Z, et al. Mesoporous hollow Sb/ZnS@ C Core-shell heterostructures as anodes for high-performance sodium-ion batteries[J]. Small, 2018, 14(16): 1704517.

[25] Feng Q, Li H, Tan Z, et al. Design and preparation of three-dimensional MnO/N-doped carbon nanocomposites based on waste biomass for high storage and ultra-fast transfer of lithium ions[J]. Journal of Materials Chemistry A, 2018, 6(40): 19479-19487.

[26] Chang Y, Zhang G, Han B, et al. Polymer dehalogenation-enabled fast fabrication of N, S-codoped carbon materials for superior supercapacitor and deionization applications[J]. ACS Applied Materials & Interfaces, 2017, 9(35): 29753-29759.

[27] Chen M, Zhang Z, Si L, et al. Engineering of yolk-double shell cube-like SnS@ N-S codoped carbon as a high-performance anode for Li- and Na-ion batteries[J]. ACS Applied Materials & Interfaces, 2019, 11(38): 35050-35059.

[28] Jing M, Chen Z, Li Z, et al. Facile synthesis of ZnS/N, S co-doped carbon composite from zinc metal complex for high-performance sodium-ion batteries[J]. ACS Applied Materials & Interfaces, 2018, 10(1): 704-712.

[29] Zhang W, Huang Z, Zhou H, et al. Facile synthesis of ZnS nanoparticles decorated on defective CNTs with excellent performances for lithium-ion batteries anode material[J]. Journal of Alloys and Compounds, 2020, 816: 152633.

[30] Park G D, Choi S H, Lee J K, et al. One-Pot method for synthesizing spherical-like metal sulfide-reduced graphene oxide composite powders with superior electrochemical properties for lithium-ion batteries[J]. Chemistry-A European Journal, 2014, 20(38): 12183-12189.

[31] Mao M, Jiang L, Wu L, et al. The structure control of ZnS/graphene composites and their excellent properties for lithium-ion batteries[J]. Journal of Materials Chemistry A, 2015, 3(25): 13384-13389.

[32] Chen Z, Wu R, Wang H, et al. Construction of hybrid hollow architectures by in-situ rooting ultrafine ZnS nanorods within porous carbon polyhedra for enhanced lithium storage properties[J]. Chemical Engineering Journal, 2017, 326: 680-690.

[33] Park A R, Jeon K J, Park C M. Electrochemical mechanism of Li insertion/extraction in ZnS and ZnS/C anodes for Li-ion batteries[J]. Electrochimica Acta, 2018, 265: 107-114.

[34] Grugeon S, Laruelle S, Dupont L, et al. An update on the reactivity of nanoparticles Co-based compounds towards Li[J]. Solid state sciences, 2003, 5(6): 895-904.

[35] Ponrouch A, Taberna P L, Simon P, et al. On the origin of the extra capacity at low potential in materials for Li batteries reacting

through conversion reaction[J]. Electrochimica Acta, 2012, 61: 13-18.

[36] Mao Y, Duan H, Xu B, et al. Lithium storage in nitrogen-rich mesoporous carbon materials[J]. Energy & Environmental Science, 2012, 5(7): 7950-7955.

[37] Balaya P, Bhattacharyya A J, Jamnik J, et al. Nano-ionics in the context of lithium batteries[J]. Journal of Power Sources, 2006, 159(1): 171-178.

[38] Augustyn V, Come J, Lowe M A, et al. High-rate electrochemical energy storage through Li^+ intercalation pseudocapacitance[J]. Nature materials, 2013, 12(6): 518-522.

[39] Zhang W, Zhou H, Huang Z, et al. 3D hierarchical microspheres constructed by ultrathin MoS_2-C nanosheets as high-performance anode material for sodium-ion batteries[J]. Journal of Energy Chemistry, 2020, 49: 307-315.

[40] Wang F, Zhang W, Zhou H, et al. Preparation of porous FeS_2-C/RG composite for sodium ion batteries[J]. Chemical Engineering Journal, 2020, 380: 122549.

[41] Wang M, Huang Y, Zhang N, et al. Fabrication of Ti^{3+} doped TiO_2 coated Mn_3O_4 nanorods with voids and channels for lithium storage[J]. Chemical Engineering Journal, 2019, 370: 1425-1433.

[42] Yu D, Pang Q, Gao Y, et al. Hierarchical flower-like VS_2 nanosheets-A high rate-capacity and stable anode material for sodium-ion battery[J]. Energy Storage Materials, 2018, 11: 1-7.